BBA - Biomembranes 1866 (2024) 184332

Contents lists available at ScienceDirect

BBA - Biomembranes

journal homepage: www.elsevier.com/locate/bbamem

# Effects induced by $\eta^6$-*p*-cymene ruthenium(II) complexes on Langmuir monolayers mimicking cancer and healthy cell membranes do not correlate with their toxicity

Ellen C. Wrobel [a,*], Ivelise Dimbarre Lao Guimarães [b], Karen Wohnrath [b], Osvaldo N. Oliveira Jr [a,*]

[a] São Carlos Institute of Physics, University of São Paulo, CP 369, São Carlos, São Paulo, SP 13560-970, Brazil
[b] Department of Chemistry, Universidade Estadual de Ponta Grossa, Ponta Grossa, Paraná 84030-900, Brazil.

ARTICLE INFO

*Keywords:*
Ruthenium-arene complexes
Langmuir monolayers
Membrane models
Cytotoxicity
Outer leaflet of plasma membrane
IDMAP

ABSTRACT

The mechanism of chemotherapeutic action of Ru-based drugs involves plasma membrane disruption and valuable insights into this process may be gained using cell membrane models. The interactions of a series of cytotoxic $\eta^6$-*p*-cymene ruthenium(II) complexes, [Ru($\eta^6$-*p*-cymene)P(3,5-C($CH_3$)$_3$-$C_6H_3$)$_3Cl_2$] **(1)**, [Ru($\eta^6$-*p*-cymene)P(3,5-$CH_3$-$C_6H_3$)$_3Cl_2$] **(2)**, [Ru($\eta^6$-*p*-cymene)P(4-$CH_3O$-3,5-$CH_3$-$C_6H_2$)$_3Cl_2$] **(3)**, and [Ru($\eta^6$-*p*-cymene)P(4-$CH_3O$-$C_6H_4$)$_3Cl_2$] **(4)**, were examined using Langmuir monolayers as simplified healthy and cancerous outer leaflet plasma membrane models. The cancerous membrane (CM1 and CM2) models contained either 40 % 1,2-dipalmitoyl-*sn*-glycero-3-phosphocholine (DPPC) or 1,2-dioleoyl-*sn*-glycero-3-phosphocholine (DOPC), 30 % cholesterol (Chol), 20 % 1,2-dipalmitoyl-*sn*-glycero-3-phosphoethanolamine (DPPE), and 10 % 1,2-dipalmitoyl-*sn*-glycero-3-phospho-L-serine (DPPS). Meanwhile, the healthy membrane (HM1 and HM2) models were composed of 60 % DPPC or DOPC, 30 % Chol and 10 % DPPE. The complexes affected surface pressure isotherms and decreased compressional moduli of cancerous and healthy membrane models, interacting with the monolayers headgroup and tails according to data from polarization-modulated infrared reflection absorption spectroscopy (PM-IRRAS). However, the effects did not correlate with the toxicity of the complexes to cancerous and healthy cells. Multidimensional projection technique showed that the complex **(1)** induced significant changes in the CM1 and HM1 monolayers, though it had the lowest cytotoxicity against cancer cells and is not toxic to healthy cells. Moreover, the most toxic complexes **(2)** and **(4)** were those that least affected CM2 and HM2 monolayers. The findings here support that the ruthenium complexes interact with lipids and cholesterol in cell membrane models, and their cytotoxic activities involve a multifaceted mode of action beyond membrane disruption.

## 1. Introduction

The discovery of the antitumor efficacy of cisplatin in the late 1960s marked a significant development in cancer therapy, increasing interest in metal-based anticancer drug candidates and their mechanisms of action [1–3]. Despite the high efficacy of cisplatin and its analogues towards several human cancers, they show considerable toxicity against non-tumor cells, causing several side effects [3–5]. Furthermore, some tumors have been reported to acquire drug resistance [6,7]. As an alternative to cisplatin and its derivatives, new drug candidates have been developed from other metals and metal ions, in particular, ruthenium complexes that can be employed against cisplatin-resistant tumors [5,8–10]. Ruthenium complexes have been demonstrated to be more effective in chemotherapy and to be less toxic against healthy cells, with some of them currently in the early stages of clinical studies [11–13], and also can act as a potent antimetastatic agent [14]. Ruthenium complexes may have many targets and mechanisms for anticancer activity, such as interference with DNA replication and transcription, enzyme inhibition, endoplasmic reticulum stress, as well as plasma membrane permeabilization [9,12,13,15,16], and their mode of action will be governed not only by ruthenium chemistry, but also by the properties of the complex ligands [9,10].

* Corresponding authors.
*E-mail addresses:* wrobel.ellen@gmail.com (E.C. Wrobel), chu@ifsc.usp.br (O.N. Oliveira).

https://doi.org/10.1016/j.bbamem.2024.184332
Received 11 March 2024; Received in revised form 8 May 2024; Accepted 9 May 2024
Available online 11 May 2024

To enter cells, the complexes must either cross or penetrate the cell membrane, which is accomplished by Ru(II) complexes through several mechanisms including passive diffusion, active transport, and endocytosis [3,5,9]. For instance, organometallic ruthenium(II) complexes containing $\eta^6$-*p*-cymene ligands are considered promising because they help stabilize ruthenium in the +2 oxidation state and enhance the complex lipophilicity, which is known to have an impact on cellular uptake [3,17–20]. Some ruthenium complexes are known to act on the cell membrane, altering its permeability and causing cell leakage and apoptosis [15,21]. Because the interaction and/or incorporation of an active drug into the cell membrane is relevant for its cytotoxicity, it is essential to comprehend the interactions between drugs and the cell membrane in detail [22]. Owing to the complexity of the cell membrane, mimetic model systems have been established to investigate anticancer drug-membrane interactions, such as the Langmuir monolayers [23–31]. Even though they only mimic half of the cell membrane, lipid Langmuir monolayers are useful due to the ability to control composition and surface packing [23,32,33].

Ruthenium complexes containing a *p*-cymene ring are known to possess antimicrobial and anticancer properties [10,34–37], and the main mechanism for the cellular uptake of Ru(II) complexes is through endocytosis [3,9]. The Ru(II)-arene complexes [Ru($\eta^6$-*p*-cymene)($PAr_3$)$Cl_2$], containing the ligands Ar = 3,5-$((CH_3)_3C)_2C_6H_3$–, 3,5-$(CH_3)_2C_6H_3$–, 4-$CH_3O$-3,5-$(CH_3)_2C_6H_2$–, and 4-$CH_3O$-$C_6H_4$–, named herein as **(1)**, **(2)**, **(3)**, and **(4)** respectively, which are strongly coordinated to the metallic center and, due to their hydrophobic properties, allow passive transport through cell membranes. In particular, complexes **(1)**, **(2)**, and **(4)** have promising anticancer activity against lung (A549) and breast (MDA-MB-231) cell lines [36]. Due to the low solubility and crystallization of **(3)** in cell media [36], we do not yet have information on its cytotoxicity. Since anticancer drugs should not harm healthy cells, complexes **(1)**, **(2)**, and **(4)** were tested against the MRC-5 human non-tumoral lung strain. Only complex **(1)** had no measurable toxicity [36].

In this paper, we investigated the effect of **(1)**–**(4)** on simplified cancer and healthy cell membrane models containing saturated and/or unsaturated lipids and cholesterol, which were represented as Langmuir monolayers, to obtain molecular-level information about their interactions. The main aim was to determine whether their cytotoxic activities are associated with the disruption of the cell membrane and to examine how these complexes interact with the proposed membrane models. Fig. 1 shows a visual representation of the goals in this study. The interaction between ruthenium complexes and cancer and healthy membrane models was explored with surface pressure-area (π–A) isotherms, Brewster angle microscopy (BAM), and polarization-modulated infrared reflection absorption spectroscopy (PM-IRRAS). Because multiple parameters affected the π-A isotherms and PM-IRRAS data, a comparison of the effects from the complexes was made by treating the data with a multidimensional projection technique [38].

## 2. Materials and methods

### 2.1. Materials

The **(1)–(4)** ruthenium complexes [Ru($\eta^6$-*p*-cymene)(P**Ar**$_3$)$Cl_2$], where **Ar** is 3,5-$((CH_3)_3C)_2C_6H_3$–, 3,5-$(CH_3)_2C_6H_3$–, 4-$CH_3O$-3,5-$(CH_3)_2C_6H_2$–, and 4-$CH_3O$-$C_6H_4$–, respectively, were synthesized and purified through a well-established route [36]. The phospholipids 1,2-dipalmitoyl-*sn*-glycero-3-phosphocholine (DPPC), 1,2-dioleoyl-*sn*-glycero-3-phosphocholine (DOPC), 1,2-dipalmitoyl-*sn*-glycero-3-phosphoethanolamine (DPPE), and 1,2-dipalmitoyl-*sn*-glycero-3-phospho-L-serine (DPPS) were acquired from Avanti Polar Lipids Inc. Cholesterol was purchased from Sigma Aldrich. The chemical structures of the Ru complexes and lipids are illustrated in Fig. 1. Chloroform used as the spreading solvent in the Langmuir monolayers experiments had HPLC grade obtained from Panreac. Methanol was purchased from Synth. The salts NaCl, KCl, $Na_2HPO_4$, and $KH_2PO_4$ for preparing the phosphate buffer saline solution (PBS, pH 7.4) were obtained from Synth, Neon or Êxodo Científica (Brazil). Ultrapure water was taken from a Millipore Milli-Q system with a resistivity of 18.2 MΩ.cm.

### 2.2. Membrane models

Phosphatidylcholine (PC), a zwitterionic lipid, is the most abundant phospholipid in the healthy membrane outer leaflet [22,39,40]. Cholesterol (Chol) is the major sterol of mammalian cell membranes, essential for maintaining structural integrity and regulating cell membrane fluidity [41,42]. Phosphatidylethanolamine (PE) is found on both outer and inner leaflets of plasma membranes. It is mostly located in the inner leaflet, but its distribution is reversed in many cancers, with a preference for the outer leaflet [22,39,43]. Phosphatidylserine (PS) is found in the inner leaflet of the cell membrane, but due to the loss of the lipid asymmetric distribution observed in several types of cancer, PS is exposed on the outer leaflet [22,43]. Hence, PE and PS lipids can be considered as cancer biomarkers since they are mostly located on the outer layer of the membrane [22,39]. Based on the information above and considering that mammalian plasma cell membranes are composed of glycerolipids (65 % mol), sphingolipids (10 % mol), and cholesterol (25 % mol) [44], we chose to model the outer leaflet of healthy (HM) plasma membrane as 60 % DPPC (or DOPC), 10 % DPPE, and 30 % Chol. The outer leaflet of cancerous (CM) plasma membrane model was composed of 40 % DPPC (or DOPC), 20 % DPPE, 10 % DPPS, and 30 % Chol [39,44–46]. In this study, we opt to investigate two types of membrane systems: one comprised solely of saturated lipids and the other incorporating an unsaturated lipid. The membrane models comprising only saturated lipids were denoted as HM1 or CM1. In contrast, those incorporating the double unsaturated lipid DOPC, instead of the saturated DPPC, were labeled as HM2 or CM2. The lipids of CM1 and HM1 models were selected based on their saturated 16-carbon tails, which ensure comparable tail properties. Additionally, the outer leaflet of the plasma membrane contains more saturated than polyunsaturated lipids [47,48], leading to a biomembrane that exhibits high rigidity, ordered structure, enhanced stability, and reduced fluidity. Due to the asymmetric lipidomic composition of the exoplasmic outer leaflet [48], which comprises both saturated and unsaturated lipids, we incorporated DOPC instead of DPPC in the CM2 and HM2 models. The inclusion of the double unsaturated lipid in the models leads to a higher level of fluidity and enhances the flexibility [49,50] of membrane models.

### 2.3. Langmuir monolayer studies

The experiments were performed using a homemade Langmuir trough coupled to a KSV NIMA instrument (KSV 5000, KSV Instruments, Ltd., Helsinki, Finland) with a 159 $cm^2$ surface area. The trough and its barriers are made of Teflon. The trough was equipped with a Wilhelmy plate made of filter paper (chromatography paper Whatman Chr1) connected to an electrobalance (resolution of 4 μN/m). The Langmuir trough was cleaned with ethanol, chloroform, and ultrapure water prior to all experiments. The trough was filled with 65 mL of phosphate-buffered saline (PBS, pH 7.4), formulated under Cold Spring Harbor Protocols [51]. Solutions containing $1 \times 10^{-3}$ mol/L of the phospholipids, cholesterol or Ru complexes were prepared using chloroform or chloroform:methanol (4:1 and 3:2 *v*/v) solutions for DPPE and DPPS. Mixed systems were prepared by combining different volumes of stock solutions of lipids, cholesterol, and Ru complexes to obtain mixed spreading solutions with 2, 5, and 15 % of Ru complexes prior to cospreading them at the air-water interface. This cospreading method was chosen to investigate how these bioactive complexes interact with the monolayers. Pure lipids, HM1, HM2, CM1, and CM2 membrane models, **(1)–(4)** Ru complexes, and HM1/Ru, HM2/Ru, CM1/Ru, and CM2/Ru mixed monolayers were spread onto the subphase containing

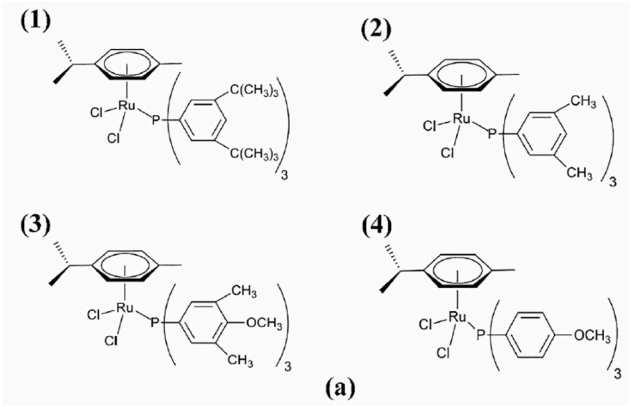


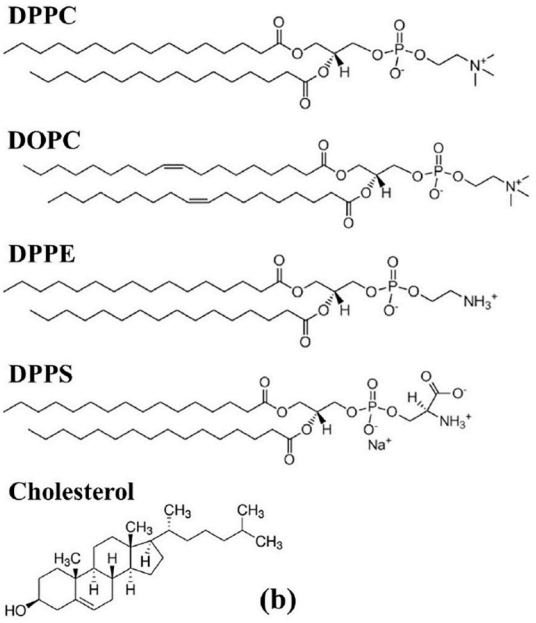


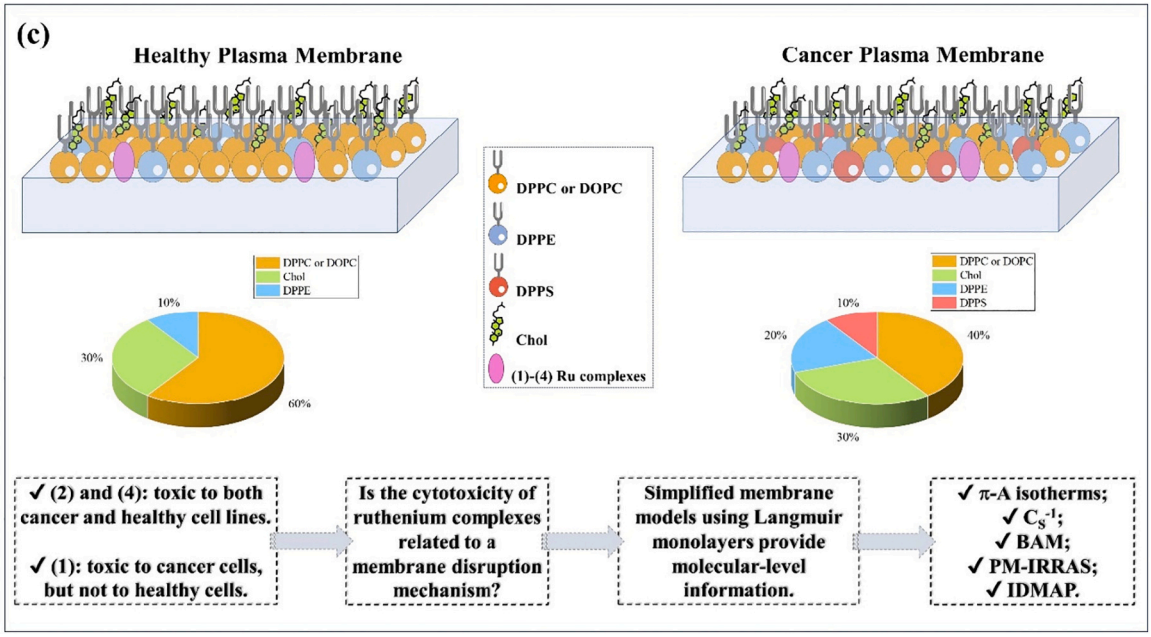


**Fig. 1.** (a) Molecular structures of ruthenium complexes **(1)** [Ru($\eta^6$-*p*-cymene)P(3,5-C($CH_3$)$_3$-$C_6H_3$)$_3Cl_2$], **(2)** [Ru($\eta^6$-*p*-cymene)P(3,5-$CH_3$-$C_6H_3$)$_3Cl_2$], **(3)** [Ru($\eta^6$-*p*-cymene)P(4-$CH_3O$-3,5-$CH_3$-$C_6H_2$)$_3Cl_2$], and **(4)** [Ru($\eta^6$-*p*-cymene)P(4-$CH_3O$-$C_6H_4$)$_3Cl_2$]; (b) structures of the membrane model compounds DPPC, DOPC, DPPE, DPPS, and cholesterol. (c) Scheme illustrating the study outline.

PBS using a Hamilton microsyringe. After 15 min for solvent evaporation, the barriers were symmetrically compressed at 10 mm/min. The Wilhelmy method was applied for measuring the surface pressure. All experiments were conducted at 22 ± 1 °C. Surface pressure *vs.* mean molecular area (π-A) were made in triplicate.

The first insight into the mechanical properties of the pure and mixed monolayers was obtained by analyzing the compressional modulus, $C_S^{-1}$, calculated from the π-A isotherm data following Eq. (1). This characterization provides information on the molecular ordering and stiffness of the monolayers, which is useful in determining the phase transition in Langmuir films [52].

$$C_S^{-1} = -A\left(\frac{\partial \pi}{\partial A}\right)_T \quad (1)$$

where $A$ is the average molecular area at a given surface pressure π.

The miscibility and molecular interactions between ruthenium complexes and cell membrane models were quantified by calculating the thermodynamic parameters of excess area ($\Delta A^E$) and excess free energy ($\Delta G^E$) of mixing for all mixed systems from their π-A isotherms. Eqs. (2)–(4) [53–56] were used for π = 15 mN/m.

$$A_{12}(\pi) = X_1 A_1(\pi) + X_2 A_2(\pi) \quad (2)$$

$$\Delta A^E = A_{exp} - A_{12} \quad (3)$$

$$\Delta G^E = N_A \int_0^{\pi} \left[A_{exp} - A_{12}\right] d\pi \quad (4)$$

where $A_{12}$ is the mean molecular area for an ideal mixture, $A_1$ and $A_2$ denote the molecular area of each single system (1 and 2) at a given surface pressure π, $X_1$ and $X_2$ represent the mole fractions of the components in the mixed film, $N_A$ is the Avogadro number, and $A_{exp}$ is the experimental area for the mixed monolayer obtained from the π-A isotherm.

The effect of **(1)**–**(4)** ruthenium complexes on the surface pressure-area isotherms for the different membrane models was also explored with the multidimensional interactive document mapping (IDMAP) projection technique [38], within the PEx-Sensors software [57]. This multidimensional projection technique was helpful for comparing the different mixed systems studied, by converting the whole π-A isotherms into single-colored dots on the map using the *Fastmap* dimension reduction algorithm. π-A isotherms ranging from 0 to 30 mN/m are represented by single data points projected on a 2D Euclidean space, where data points close to each other correspond to similar isotherms using Euclidean distances. The silhouette coefficient (S) values, which range from −1 to 1, were used to assess the projection's quality, with higher values implying greater quality of data discrimination [57]. Using the ImageJ software, the relative Euclidean distances were determined from the maps to examine the effect of the different ruthenium complexes on the membrane models.

### 2.4. Brewster angle microscopy

Brewster angle microscopy (BAM) images were taken with an ellipsometer Accurion EP4 (Accurion, Göttingen, Germany) coupled to a KSV Nima Langmuir trough. The BAM apparatus is equipped with an ultra-objective camera SVS-Vistek eco 285 and 50 mW laser emitting *p*-polarized light at 658 nm with 100 % of power. For all measurements, the incident angle was 53.1°, with the polarizer, analyzer, and compensator set to 2.0, 10.0, and 0.0° respectively. Further information concerning the BAM technique is found in refs. [58,59]. The images were corrected using the DataStudio software, with the greyscale adjusted for images with excessive brightness. BAM was used to monitor changes in monolayer morphology caused by **(1)**–**(4)** insertion on membrane models. BAM experiments were carried out for the **(1)**–**(4)** complexes, healthy and cancer membrane models, as well as for the effect of 15 % of the complexes on the membrane models. The monolayers were compressed at a rate of 10 mm/min. Images were acquired at several surface pressures.

### 2.5. Polarization-modulation infrared reflection absorption spectroscopy

Polarization-modulated infrared reflection-absorption spectroscopy (PM-IRRAS) experiments were carried out in a KSV PMI 550 Instrument (KSV Instruments, Ltd., Helsinki, Finland) installed over a Mini KSV Langmuir, with polarization modulated between *p* and *s* at a high frequency. The incidence angle was set to 81°. Each spectrum was acquired with 600 scans with a spectral resolution of 8 $cm^{-1}$. The spectra were taken for the healthy and cancerous membrane models, and for the aforementioned monolayers containing 15 % of ruthenium complexes at 30 mN/m. The spectra for pure **(1)**–**(4)** films were acquired at 15 mN/m, as the collapse process for these monolayers is observed at pressures below 30 mN/m. The reproducibility of the spectra was ensured by performing each experiment at least two times.

## 3. Results and discussion

### 3.1. Langmuir monolayers of [Ru($\eta^6$-*p*-cymene)(PAr$_3$)Cl$_2$] complexes

The behavior of **(1)**–**(4)** ruthenium complexes bearing a *p*-cymene ligand on PBS subphases was investigated with surface pressure-area (π-A) isotherms, shown in Fig. 2a. These complexes formed monolayers with limiting areas ($A_0$) of 151, 131, 165, and 95 $Å^2$ for complexes **(1)** through **(4),** respectively. $A_0$ was calculated by extrapolating a tangent line from the pressure − area curve of the more ordered phase to zero pressure. The collapse pressure for complexes **(1)**, **(2)**, **(3)**, and **(4)** begins at approximately 27, 20, 16, and 9 mN/m, respectively. The limiting area, collapse pressure, and the shape of π-A isotherms are similar to those in the literature [36]. The maximum compressional modulus ($C_S^{-1}$) in Fig. 2b decreases from **(1)** to **(4)**, where **(1)**–**(3)** complexes are in the liquid-expanded phase and the complex **(4)** only reaches a low-density liquid phase [33]. The maximum compressional modulus is achieved at surface areas of approximately 128, 105, 139, and 79 $Å^2$, which are lower than the respective limiting areas for complexes **(1)** through **(4)**. This pattern may indicate a shift from a more expanded to a more compressed molecular state. The higher $C_S^{-1}$ for **(1)** and consequently the formation of less compressible monolayers [33] are associated with its globular structure, which was determined by X-Ray crystallography [36]. Although complexes **(1)** and **(2)** exhibit a similar globular structure, the presence of a more lipophilic substituent in complex **(1)** [36] results in a more close packing at the interface. At low pressures, **(1)**–**(4)** complexes exhibit similar morphological behavior, as shown in the BAM images in Fig. S1 in the SI. Small domains (bright points) dispersed in the liquid-expanded phase (dark regions) are seen at low pressures, which tend to aggregate as the surface pressure increases. At 25 mN/m, BAM images for **(1)** and **(2)** show a significant increase in the number of 3-dimensional aggregates, which is consistent with their collapse mechanisms. **(3)** and **(4)** displayed strong aggregation at low pressures, as their methoxy groups likely lead to less stable monolayers with 3-dimensional aggregates. This is driven by a combination of competing van der Waals interactions – comprising van der Waals-Keesom (orientation forces), van der Waals-Debye (induced forces), and van der Waals-London (dispersion forces) [60] – alongside hydrogen bonding between water molecules from the subphase and the oxygen atom of the -OMe group [36], inducing collapse processes at lower pressures. In contrast, the more lipophilic **(1)** has higher stability at the interface, which delays its aggregation and eventual collapse. The non-amphiphilic nature of the complexes is consistent with their low values of collapse pressure and aggregation even at low pressures.

Fig. S2 in SI shows the PM-IRRAS spectra for neat **(1)**–**(4)** at 15 mN/m. The band at ~2990 $cm^{-1}$ is assigned to the aromatic rings of $\eta^6$-*p*-cymene ligands ($\nu$(HC=CH)). The bands at 2840–2960 $cm^{-1}$ are due to

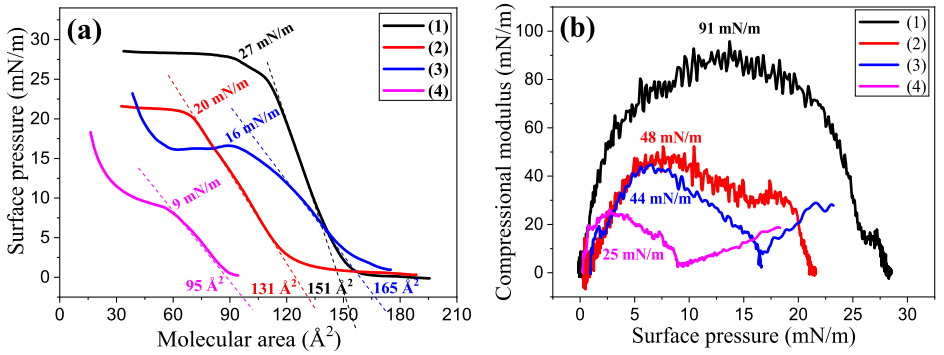


**Fig. 2.** Surface pressure-area (π-A) isotherms (a) and surface compressional modulus ($C_S^{-1}$) (b) for **(1)**–**(4)** monolayers on PBS subphase (pH = 7.4).

asymmetric stretching ($\nu Csp^3$-H) of the methyl group of *p*-cymene and $PAr_3$ ligands. The bands at ~1560 and ~ 1490 $cm^{-1}$ are assigned to the C═C in plane asymmetric stretching. The band at ~1260 $cm^{-1}$ is related to C—H asymmetric stretching (νC-H) in methyl and isopropyl substituents in the aromatic ring. The band at ~1280 $cm^{-1}$ in the spectra for **(3)** and **(4)** is attributed to the asymmetric stretching of O-$CH_3$ ($\nu_{as}$C-O) substituent. The coordination of phosphine ligands to the complexes was supported by the bands around 1100 $cm^{-1}$, which is assigned to the asymmetric stretching of the P—C bond [35,36]. The band around ~1675 $cm^{-1}$, which is attributed to the bending mode of water ($\delta H_2O$) [61], has a quite high intensity for complexes **(1)** and **(2)**. Conversely, complexes **(3)** and **(4)** display a significant reduction in its intensity. This band is associated with the complex moiety in contact with water at the interface, and differences in its intensity provide evidence of variations in hydration levels within the analyzed complexes at the interface. This observation aligns with the lower stability of these monolayers observed in the isotherms and BAM images (Figs. 2 and S1 in SI). These studies revealed that the ruthenium complexes exhibit surface activity and can form Langmuir despite having non-amphiphilic structures.

### 3.2. Membrane models

The surface pressure-area isotherms and compressional modulus data for pure DPPC, DOPC, cholesterol, DPPE, and DPPS on PBS subphase (pH = 7.4) are shown in Fig. S3 in SI, being consistent with the literature [30,62–65]. The limiting area and maximum compressional modulus are 57, 85, 42, 55, and 56 $Å^2$, and 220, 80, 312, 305, and 201 mN/m for DPPC, DOPC, Chol, DPPE, and DPPS, respectively. The π-A isotherms for the selected cancerous and healthy plasma membrane models are shown in the Fig. 3a. Regarding the models comprising only

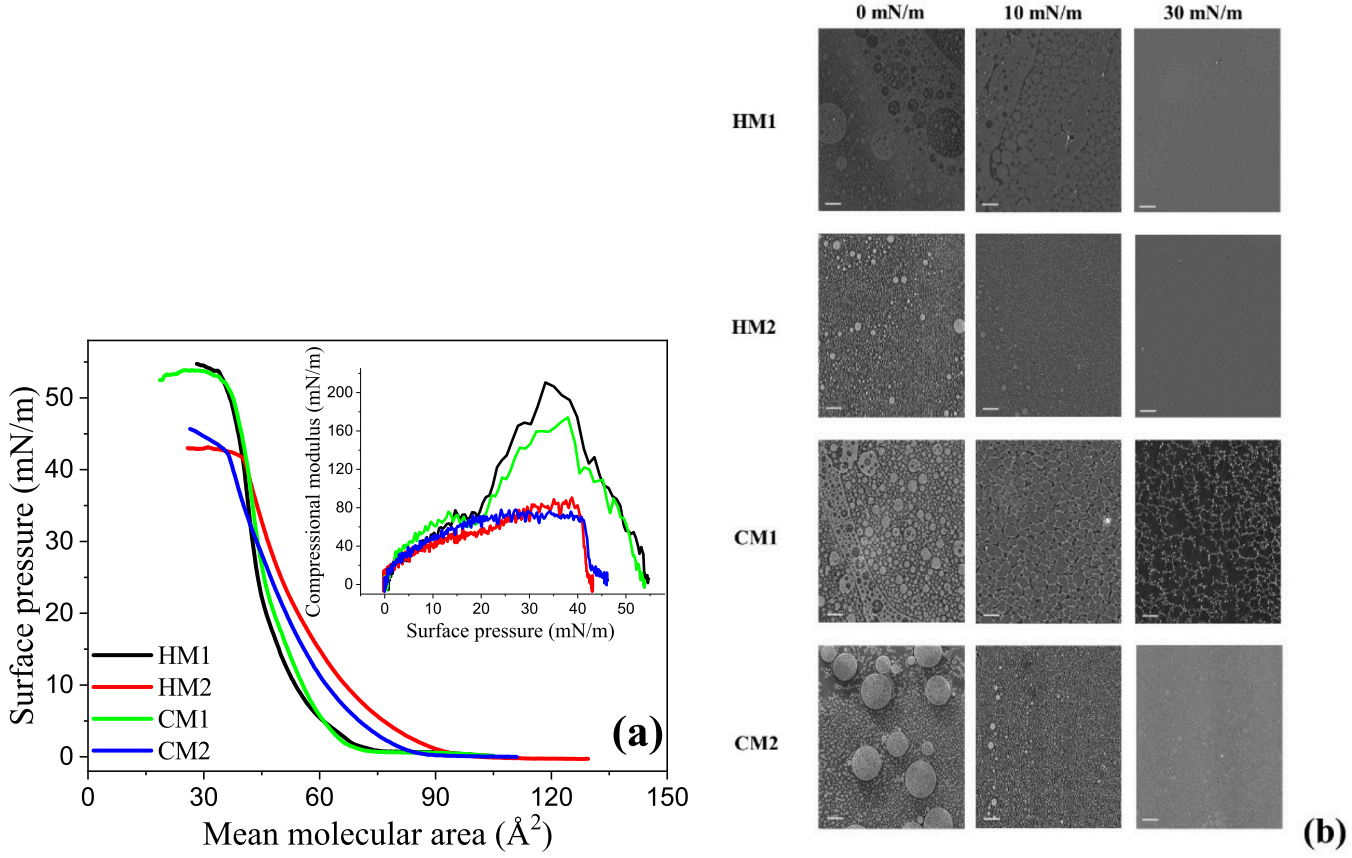


**Fig. 3.** Surface pressure-area isotherms and surface compressional modulus ($C_S^{-1}$) for monolayers of healthy (HM1 and HM2) and cancerous (CM1 and HM2) membrane models (a). BAM images at the indicated surface pressures, whose scale bar represents 50 μm (b).

saturated lipids, the extrapolated molecular areas were 52.6 and 54.5 Å$^2$ for HM1 and CM1 respectively, lying between the areas for pure lipids and cholesterol. Because pure DPPC, DPPE, and DPPS lipids have similar extrapolated molecular areas, the similarity in the π-A isotherms for CM1 and HM1 models is not surprising. In contrast to neat DPPC, the isotherms for CM1 and HM1 membrane models show no coexistence region of liquid-expanded and liquid- condensed (LE-LC) phases. Concerning the models incorporating the unsaturated DOPC lipid, namely HM2 and CM2, their isotherms are situated between those of the pure DOPC and Chol monolayers. The extrapolated molecular areas for these models are 69.1 and 67.1 Å$^2$. The molecular area of the CM2 model is consistent with the decreased molar ratio of DOPC present within this model. The maximum surface compressional modulus for HM1, CM1, HM2, and CM2 is 211, 175, 95, and 77 mN/m, respectively. It has been reported in the literature that cholesterol tends to condense lipid monolayers, particularly at higher cholesterol concentrations [66–69]. Similar to our findings, Dana-Marie Telesford et al. [66] reported that cholesterol concentrations ranging from 0.1 to 0.3 have no significant effect on the compressional modulus of DPPC monolayers. As for the models containing unsaturated lipids, it is established that the cholesterol-induced ordering effect is relatively diminished in contrast to systems comprising solely saturated lipids [70], as observed in the $C_S^{-1}$ data. At the biologically relevant pressure (~30mN/m) [71], the mean molecular area for HM1, CM1, HM2, and CM2 is 42.6 and 44.1,

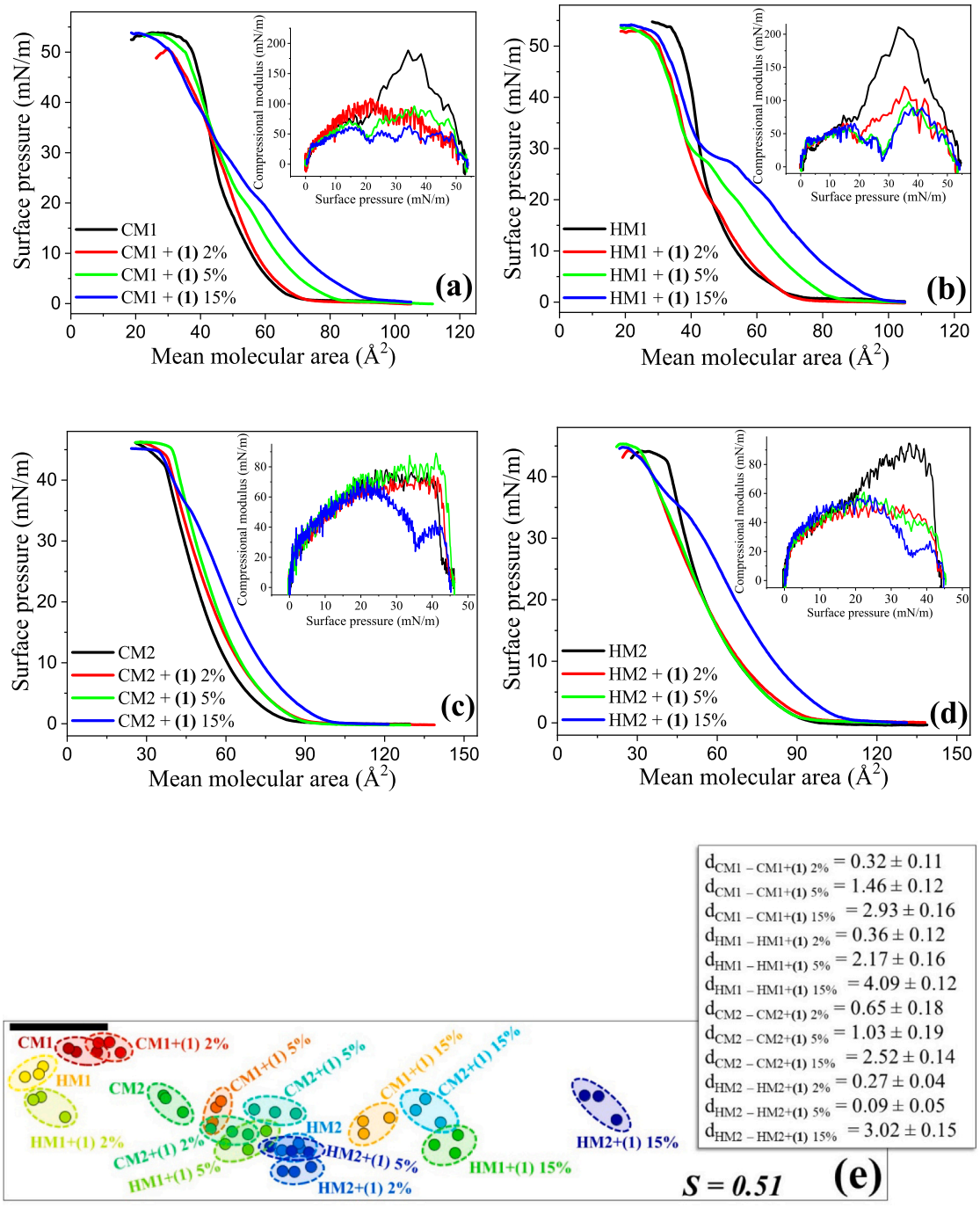


**Fig. 4.** Surface pressure-area (π-A) isotherms and surface compressional modulus ($C_S^{-1}$) for monolayers of (a, c) cancerous (CM1 and CM2) and (b, d) healthy (HM1 and HM2) membrane models, pure or mixed with 2, 5, and 15 % in mol of **(1)**; IDMAP plot (e) for the referred π-A isotherms at the pressure range of 0–30 mN/m. The black bar is a reference for measuring relative distances between the data points while disregarding scales on the axes.

46.6, and 43.6 Å$^2$, and the $C_S^{-1}$ is 170, 150, 83, and 75 mN/m, respectively.

The morphology of membrane models is influenced by their lipid composition, as depicted in Fig. 3b. The HM1 monolayer exhibits small circular domains dispersed on a fluid phase at π = 0 mN/m. These images are due to the coexistence of liquid-expanded/liquid-condensed transition phases. Upon further compression, the domains coalesced and the monolayer became homogenous, reaching a condensed phase. After π = 20 mN/m, small dots appeared over the condensed phase, which may correspond to domains rich in cholesterol. For CM1 at π = 0 mN/m, close to the lift-off in the π-A isotherm, liquid-expanded circular domains appear dispersed in a less ordered phase (dark regions). Upon further compression, the liquid-expanded domains coalesced, and liquid-condensed interconnected chain-like structures arose. This is most likely associated with the changes in intermolecular interactions within the membrane model caused by DPPS. The domains increase with additional compression up to the collapse point.

The substitution of DPPC for DOPC causes minor changes in the morphological characteristics of both healthy and cancer membrane models. In models featuring the unsaturated lipid DOPC, namely HM2 and CM2, similar behaviors were observed when compared to models incorporating the saturated DPPC lipid. These models also exhibited circular domains dispersed within a fluid phase at π = 0 mN/m, which were larger than those observed in HM1 and CM1 models. The domains coalesced and the monolayers became homogeneous as they were compressed further. Importantly, when compared to HM1 and CM1, this shift to a more homogeneous phase occurred at lower surface pressures in HM2 and CM2 models. These findings imply that the lipid composition, particularly the inclusion of DOPC, impacts the morphological dynamics and surface compressional modulus of both healthy and cancer membrane models.

### 3.3. Interaction of cancer (CM) and healthy membrane (HM) models with ruthenium complexes

The comparison of the effect of 2, 5, and 15 % of **(1)**–**(4)** on the CM1, CM2, HM1, and HM2 models is shown in Figs. S4-S6 in SI, with the main changes summarized in Tables S1 and S2 in SI. Complex **(1)** shifts the π-A isotherms of CM1 and CM2 to larger areas, in particular at higher ruthenium complex contents (Fig. 4a and c). For the CM1, this occurs mainly at low pressures as **(1)** is incorporated in the liquid-expanded monolayer, which is consistent with the larger liquid-expanded circular domains that do not fully coalesce as observed in the BAM images (Fig. S7 in SI). A squeezing out process, inferred from a plateau at 21 mN/m in the isotherm, may explain the aggregation shown in the BAM images from this pressure (Fig. S7 in SI). This implies that the monolayer components are miscible in the pressure region below collapse for **(1)**, and some molecules are eliminated from the CM1 monolayer. Hence, not all molecules are able to either cross or disrupt the cell membrane. The isotherms for the mixed monolayers containing 2, 5, and 15 % of **(1)** cross with that of pure CM1 at around 35 mN/m, consistent with the idea of its expelling from the interface. The compressional moduli in the inset in Fig. 4a indicate a significant decrease in the elasticity of the CM1 monolayer due to the interaction with complex **(1)**. The impact of **(1)** on the CM2 model yields distinct outcomes (Fig. 4c). Specifically, increasing the molar ratio of **(1)** leads to a monotonic increase in molecular area, devoid of any discernible expelling phenomenon. The introduction of complex **(1)** influences the morphological characteristics of CM2 (Fig. S8 in SI), hindering the coalescence of liquid-expanded circular domains, even under high surface pressures. Furthermore, the impact of this ruthenium complex on the mechanical properties of CM2 appeared to be almost negligible, as indicated by the minor changes in $C_S^{-1}$ values. The presence of the unsaturated DOPC lipid in CM2 contributes to a higher fluidity, thereby resulting in less pronounced changes in the mechanical properties of the membrane model upon the introduction of the complex.

As observed for the CM1 model, the π-A isotherms in Fig. 4b for HM1 containing 5 and 15 % of **(1)** are displaced to larger molecular areas compared to the neat HM1 model. Up to 28 mN/m, the mean molecular area increases; however, at higher pressures the isotherms reach a smaller area than the HM1 model itself. By increasing the molar ratio of **(1)**, the phase transition between 27 and 30 mN/m becomes more pronounced. This behavior may indicate that some **(1)** molecules are reorganizing on top of the HM1 monolayer, being gradually expelled from the HM1 matrix. Therefore, there is significant aggregation at 30 mN/m, as seen in the BAM images (Fig. S9 in SI) [72]. As complex **(1)** only impacts the HM1 monolayer significantly at π below 27 mN/m, the molecules cannot disrupt the membrane in the biologically relevant pressure regime. The lack of toxicity of complex **(1)** towards healthy cell lines may be associated with this behavior. The interaction between HM1 and **(1)** leads to a considerable decrease in the surface compressional moduli (Inset in Fig. 4b), especially at around 30 mN/m, consistent with the squeezing-out process. The introduction of **(1)** yields distinct effects on the HM2 model. Notably, at low molar ratios of **(1)**, the HM2 π-A isotherm remains unaffected up to ~25 mN/m. However, at higher pressures, the isotherms exhibit a reduced area compared to the HM2 model. In the HM2 monolayer containing 15 % of **(1)**, there is a discernible shift towards higher molecular area, implying the potential incorporation of the ruthenium complex into the monolayer. Similarly to the system involving CM2 and **(1)**, the insertion of **(1)** influences the morphology of HM2 monolayers (Fig. S10 in SI), impeding the coalescence of the liquid-expanded circular domains. This behavior suggests that the ruthenium complex can alter the cohesive forces between molecules within the monolayer, preventing domain coalescence through an influence on intermolecular interactions. The interaction between HM2 and **(1)** is further evidenced by a decrease in $C_S^{-1}$, particularly at surface pressures above 20 mN/m.

Because there are multiple π-A isotherms to compare, we employed the multidimensional projection technique IDMAP to investigate the effects caused by the Ru complexes. The key benefit of employing IDMAP is the ability to compare entire isotherm regions and translate all ruthenium-induced changes, instead of just using specific molecular areas and collapse pressure values [64]. Fig. 4e exhibits IDMAP plots for the CM1, CM2, HM1, and HM2 monolayers containing complex **(1)** at the range of 0–30 mN/m. The IDMAP map reveals that **(1)** induced significant changes on all studied monolayers, with the associated data points being far apart. The silhouette coefficient (S) was 0.51, which means a meaningful data discrimination value [73]. The relative Euclidean distances in the inset of Fig. 4e between isotherms without and with **(1)** allow us to compare the induced effects directly. A higher separation of the clusters is observed as the molar ratio of **(1)** increases, with a larger effect for the HM1 and HM2 monolayers containing 15 %.

For complex **(2)**, there is an increase in CM1 area in Fig. 5a as their molar ratio increased and the isotherm profile changed when the content reached 15 %. Inserting 2 % of **(2)** has a small effect on the mechanical properties of CM1. When 15 % of **(2)** were incorporated, the surface compressional modulus at 30 mN/m was reduced from 150 to 34 mN/m. The morphology of CM1 is changed by the inclusion of complex **(2)**, as shown in Fig. S7 in SI. Interconnected chain structures are observed at 10 mN/m, which become more pronounced with compression and eventually form a non-homogeneous film at 30 mN/m. The impact of **(2)** on CM2 (Fig. 5c) is comparatively less pronounced than that observed for CM1. A subtle increase in molecular area as **(2)** molar ratio increased, accompanied by a slight decrease in $C_S^{-1}$. These differences in comparison to CM1 could be attributed to the presence of DOPC instead of DPPC in the membrane models. Specifically, the Ru complex appears to exert a more significant effect on rigid monolayers composed solely of saturated lipids and cholesterol, as opposed to fluid monolayers containing unsaturated lipids. This suggests that the complexes may be inserted into CM2 monolayers without significantly affecting the organization of the lipids.

Complex **(2)** causes a meaningful increase in area of HM1 monolayer

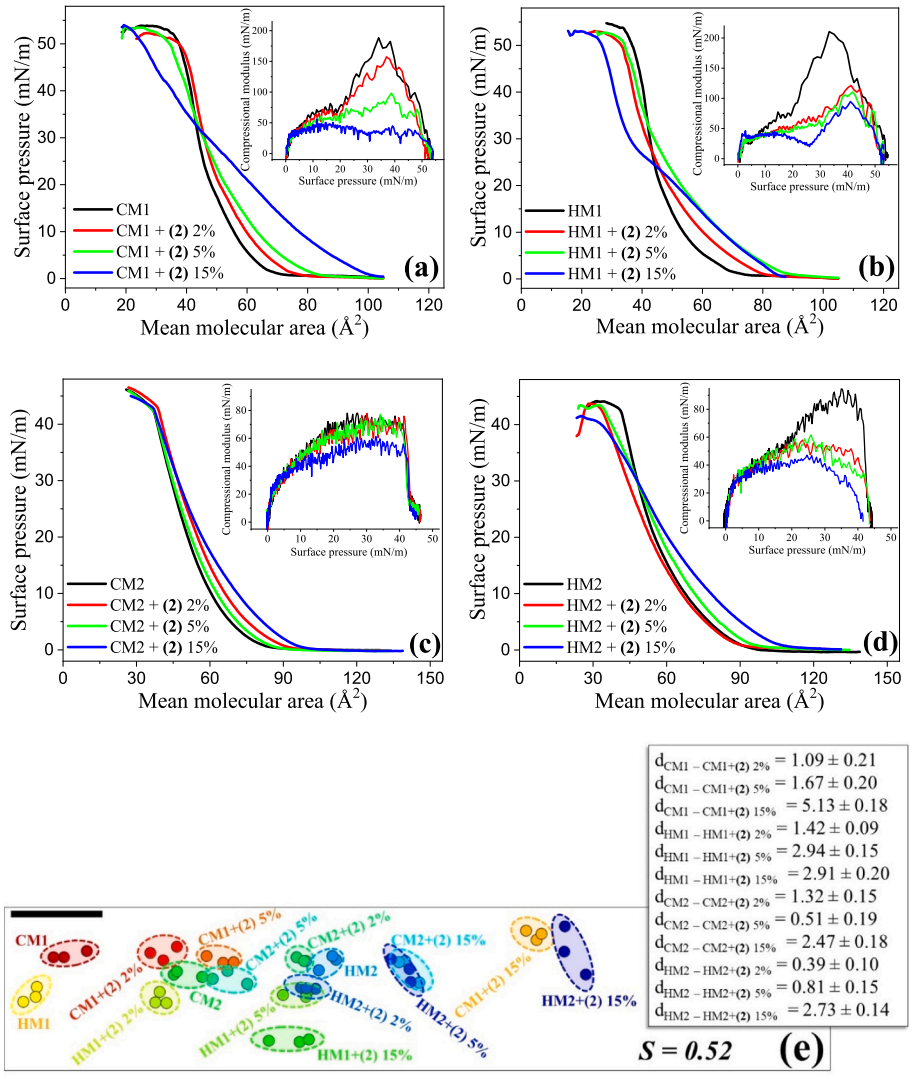


**Fig. 5.** Surface pressure-area (π-A) isotherms and surface compressional modulus ($C_S^{-1}$) for monolayers of (a, c) cancerous (CM1 and CM2) and (b, d) healthy (HM1 and HM2) membrane models, pure or mixed with 2, 5, and 15 % in mol of **(2)**; IDMAP plot (e) for the referred π-A isotherms at the pressure range of 0–30 mN/m. The black bar is a reference for measuring relative distances between the data points while disregarding scales on the axes.

(Fig. 5b), and the probable repulsive interactions are likely related to the well-distributed bright spots found in the BAM images from 20 mN/m (Fig. S9 in SI). This shift to higher molecular areas is probably correlated with the inclusion of complex **(2)** among the alkyl chains of the HM1 lipids (see below in the discussion of spectroscopic measurements). The incorporation of 15 % of complex **(2)** changes the HM1 isotherm profile significantly, and a phase transition appears at ~25 mN/m. This may indicate saturation of incorporation of **(2)** in HM1, with some molecules being expelled from the interface. Due to the incorporation of complex **(2)**, the HM1 monolayer was no longer liquid-condensed, being rather liquid expanded. Hence, significant changes were induced by complex **(2)** on HM1 monolayers even at low molar ratios. The incorporation of **(2)** into the HM2 model results in a slight increase in molecular area, although not to the extent observed in HM1. Also, the isotherm profile for HM2 was altered, accompanied by a decrease in $C_S^{-1}$ values. The BAM images in Fig. S10 in SI indicate that the incorporation of **(2)** also hinders the coalesce of circular domains, a phenomenon observed in monolayers containing other complexes (see discussion in SI). The relatively minor effects induced by **(2)** on HM2 in comparison to HM1 may be explained by the composition of the membrane models; HM2 comprised 60 % of an unsaturated lipid, which likely contributes to the fluidity of the system and, consequently, influences on the impact of the complex on the monolayer. The IDMAP plot in Fig. 5e confirms that complex **(2)** caused important changes on CM1, CM2, HM1, and HM2 monolayers, with a silhouette coefficient (S) of 0.52. Euclidean distance values are more significant for the CM1 monolayers containing **(2)**.

Complex **(3)** had a substantial impact on the CM1 monolayers (Fig. 6a), even at a low molar ratio, causing an increase in molecular area as the molar ratio of **(3)** was increased. The impact of **(3)** on the morphology of the CM1 monolayer was comparable to that induced by complex **(2)** (Fig. S7 in SI). The incorporation of **(3)** into CM1 monolayer significantly affects its mechanical properties, and the presence of 15 % of **(3)** decreased the surface compressional modulus at 30 mN/m from 150 to 52 mN/m. This increase in elasticity suggests that complex **(3)** may disrupt lipid ordering in CM1. Regarding the CM2 model (Fig. 6c), complex **(3)** increases its molecular area, but without a discernible correlation with the molar ratio. The mechanical properties of the monolayer remain practically unaltered, as indicated by the absence of substantial changes in the $C_S^{-1}$ values. The effect of **(3)** on the morphology of the CM2 monolayer was similar to that induced by complex **(2)** (Fig. S8 in SI).

Adding complex **(3)** to the HM1 monolayer shifted its π-A isotherm to larger molecular areas, Fig. 6b. These changes were accompanied by the formation of a non-homogeneous monolayer with some 3D aggregates in

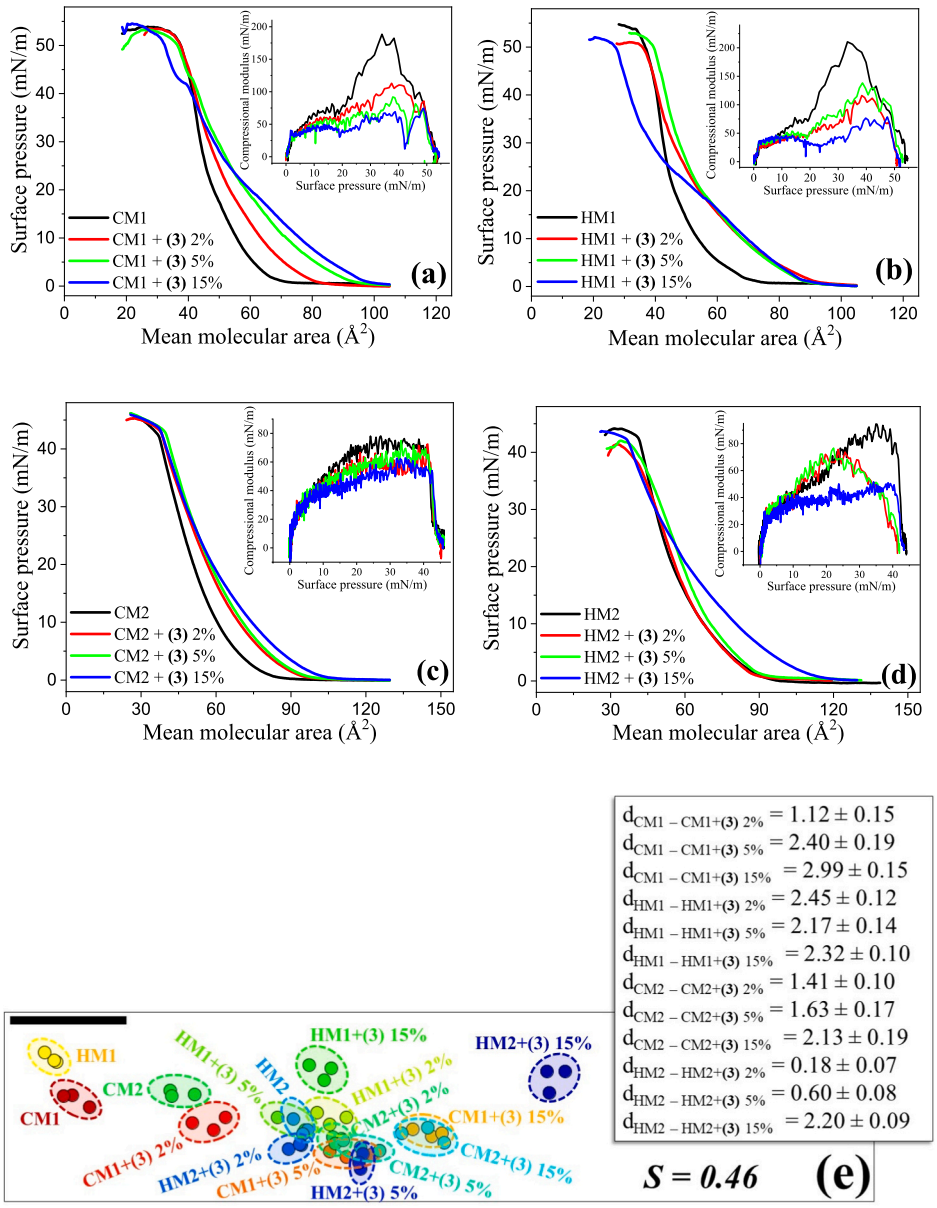


**Fig. 6.** Surface pressure-area (π-A) isotherms and surface compressional modulus for monolayers of (a, c) cancerous (CM1 and CM2) and (b, d) healthy (HM1 and HM2) membrane models, pure or mixed with 2, 5, and 15 % in mol of **(3)**; IDMAP plot (e) for the referred π-A isotherms at the pressure range of 0–30 mN/m. The black bar is a reference for measuring relative distances between the data points while disregarding scales on the axes.

the BAM images (Fig. S9 in SI). The molecular area for HM1 monolayers containing 2 % and 5 % of **(3)** coincided as the compression increased up to ~25 mN/m. The HM1 monolayers containing 15 % of **(3)** had their isotherm profile changed, indicating that the complex modifies the lipid packing, most likely caused by the presence of methoxy groups in the complex structure. Also, a plateau was observed at *ca.* 22 mN/m, which may be explained with some **(3)** molecules being expelled from the monolayer. At the pressure in the membrane environment, the $C_S^{-1}$ significantly decreased from 170 to 67, 88, and 37 mN/m for the increasing concentration of **(3)**. When examining the impact of complex **(3)** on the HM2 model (Fig. 6d), one notes that only at the highest molar ratio studied does a substantial impact on both the π-A isotherm and the compressional modulus. This highlights the significant impact of the composition of the membrane model on its interactions with the complexes. A membrane model with a higher proportion of unsaturated lipids appears to better "accommodate" the ruthenium complexes, minimizing significant disruptions to molecular organization, especially at lower concentrations. The IDMAP plot depicted in Fig. 6e yielded a silhouette coefficient S = 0.46, indicating some distinction between the clusters. This could have occurred because of isotherm overlap, particularly in models featuring DOPC. As a result, the influence of **(3)** may not have been as pronounced in these cases. Euclidean distance values are more significant in CM1 monolayers with **(3)**.

The interaction between complex **(4)** and CM1 differs from that of other complexes. Fig. 7a shows that 2 % of **(4)**, for instance, shifts the CM1 π-A isotherm to smaller areas, but it was not a condensation effect because $C_S^{-1}$ decreased. This shrinkage of the monolayer may be related to molecular accommodation of **(4)** during compression. 5 and 15 % of **(4)** shifted the CM1 isotherm to higher areas and decreased $C_S^{-1}$. As observed for **(2)** and **(3)**, complex **(4)** induced to a formation of a non-homogeneous CM1 monolayer at around 30 mN/m (Fig. S7 in SI). Complex **(4)** increased the molecular area of the CM2 model in Fig. 7c, even at the smallest molar ratio evaluated. However, there was no discernable change in $C_S^{-1}$ values. The effect of **(4)** on the morphological

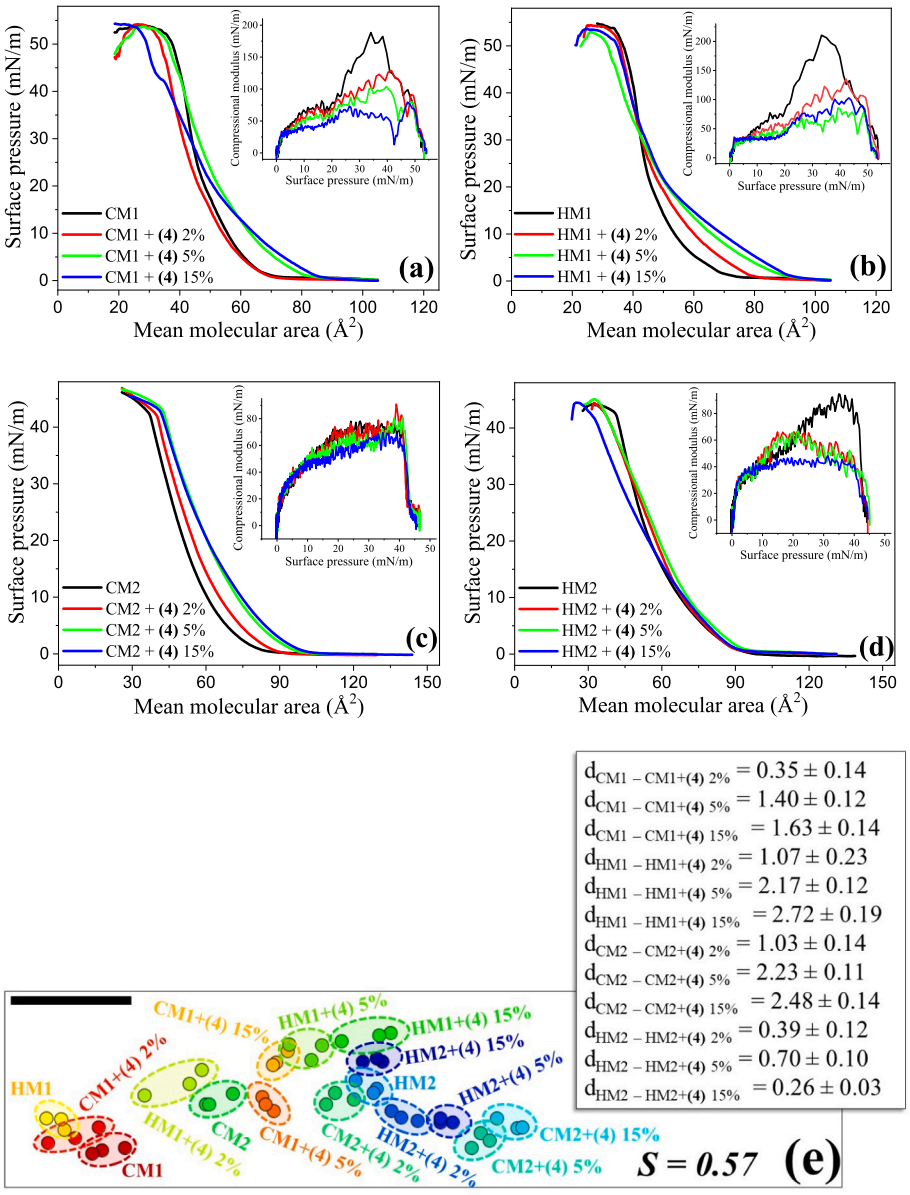


**Fig. 7.** Surface pressure-area (π-A) isotherms and surface compressional modulus for monolayers of (a, c) cancerous (CM1 and CM2) and (b, d) healthy (HM1 and HM2) membrane models, pure or mixed with 2, 5, and 15 % in mol of **(4)**; IDMAP plot (e) for the referred π-A isotherms at the pressure range of 0–30 mN/m. The black bar is a reference for measuring relative distances between the data points while disregarding scales on the axes.

properties of CM2 was consistent with the findings for the other complexes under consideration (Fig. S8 in SI). The incorporation of 2–15 % of **(4)** into the HM1 monolayer changed the π-A isotherm in Fig. 7b, causing an expansion in area at low pressures (up to ~25 mN/m). At 30 mN/m, **(4)** did not impact the π-A isotherm HM1 monolayer significantly, but $C_S^{-1}$ decreased from 170 to 90, 59, and 61 mN/m when 2, 5, and 15 % were added. Examining the influence of **(4)** on the HM2 model revealed no substantial changes in molecular area values, even at the highest proportion of the complex. However, a decrease in $C_S^{-1}$ values was noted, attributed to a modification in the profile of HM2 isotherms resulting from the inclusion of **(4)**. The IDMAP plot in Fig. 7e had a silhouette coefficient S = 0.57. The Euclidean distances depicted in the inset indicated that the HM1 model was the most affected by **(4)**.

We have also produced IDMAP plots to compare isotherms of CM1, CM2, HM1, and HM2 incorporating the three tested concentrations of the complexes. The plots are shown in conjunction with the isotherms in Figs. S4-S6 in SI. A silhouette coefficient S = 0.46 suggests a weak discrimination between the results for the effect of 2 % of the complexes in all studied models, as shown by the IDMAP plots. Complexes **(2)** and **(3)** at 2 % had the largest impact on all models at this molar ratio, as evidenced by their large Euclidean distances, except for the model HM2, which is more impacted by complex **(4)**. Upon analyzing the largest molar ratio of ruthenium complexes under study (15 %), we observed a greater differentiation of the results, as reflected by a silhouette coefficient S = 0.58. The largest effects on the CM1 model were induced by complexes **(2)** and **(3)**, the HM1 by **(1)** and **(3)**, the CM2 by **(3)**, and HM2 by **(1)** and **(3)**. The smallest effects were induced by complex **(4)** on CM1, by **(2)** and **(4)** on HM1, by **(2)** on CM2, and by **(4)** on HM2. It is clear that – overall – these results do not correlate with the toxicity of the complexes (IC50 from MTT assays [36]), because complex **(1)**, the non-toxic complex towards healthy cell line, has the most impact on the HM1 and HM2 model. Complexes **(2)** and **(4)**, the most toxic compounds against the healthy cell line, had the smallest effects on HM1 and HM2 monolayer (smaller Euclidean distances). Complex **(3)**, for which we lack cytotoxicity data, demonstrated the biggest impact on all studied models, notably at 2 and 5 % (as evidenced by the highest Euclidean

distances), suggesting its interaction with the membrane. These findings imply that the complexes indeed interact with the investigated membrane models, although their mechanism of action is not primarily due to cell membrane disruption. This conclusion was supported with further analysis of thermodynamic parameters of CM1, CM2, HM1, and HM2 monolayers, for which we calculated the excess area ($\Delta A^E$) and excess free energy ($\Delta G^E$) [53,55,68]. The results and their discussion are given in Figs. S11 and S12 in SI.

The lack of correlation between toxicity and effects on the cancer and healthy monolayers was also supported by the PM-IRRAS study whose spectra are shown in Fig. 8 with the band assignment given in Tables S3 and S4 in SI. The changes induced by the complexes originated from their interaction with CM1, CM2, HM1, and HM2 monolayers both in the headgroups – seen in the spectral region from 900 to 1800 $cm^{-1}$ -

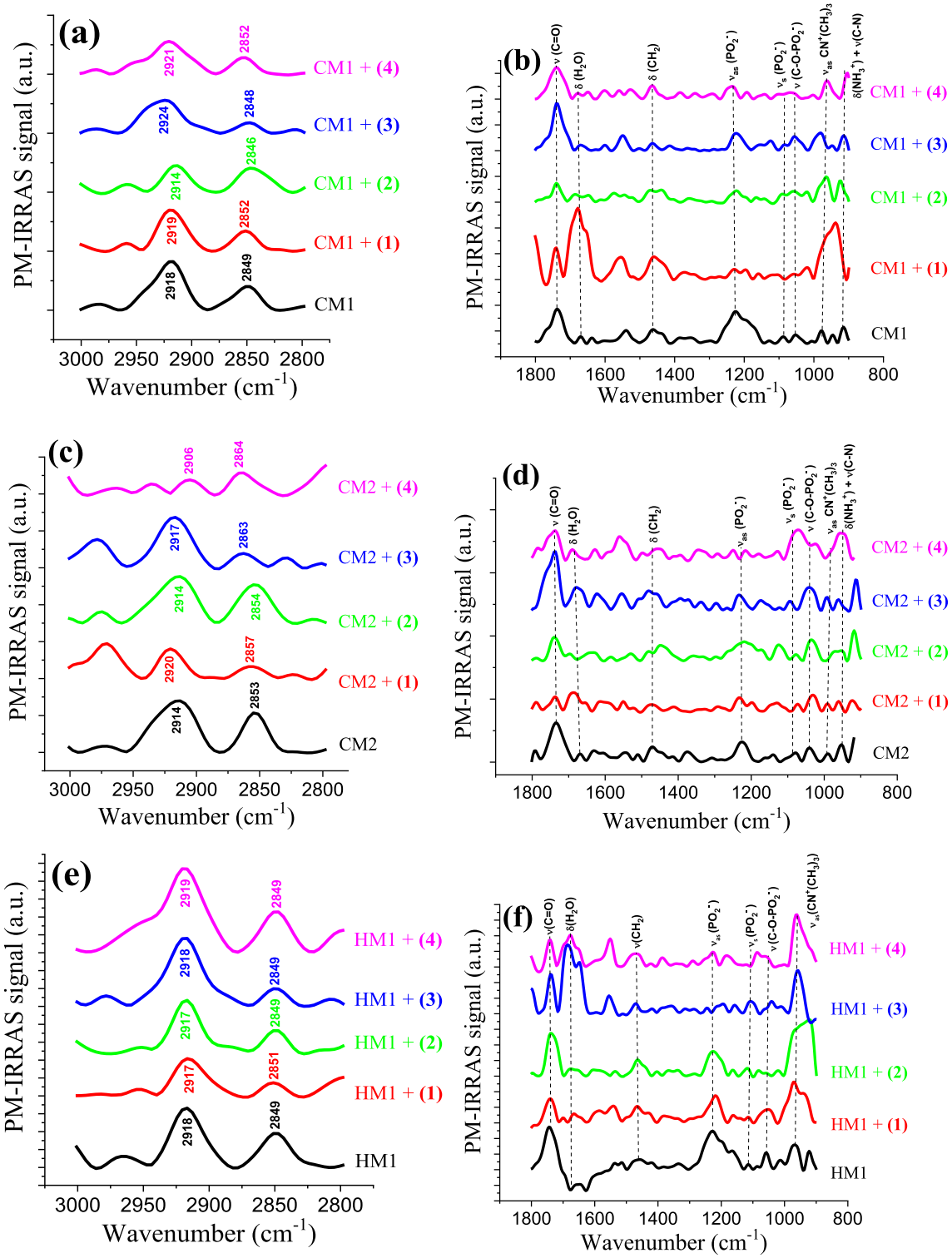


**Fig. 8.** PM-IRRAS spectra for the monolayers of CM1 (a and b), CM2 (c and d), HM1 (e and f), and HM2 (g and h) models with or without the ruthenium complexes (**(1)**–**(4)**, 15 % in mol at $\pi = 30$ mN/m, in the range of 3000–2800 and 1800–900 $cm^{-1}$; IDMAP plots for the PM-IRRAS in the range of 3000–2800 (i) and 1800–900 $cm^{-1}$ (j). The black bar is a reference for measuring relative distances between the data points while disregarding scales on the axes.

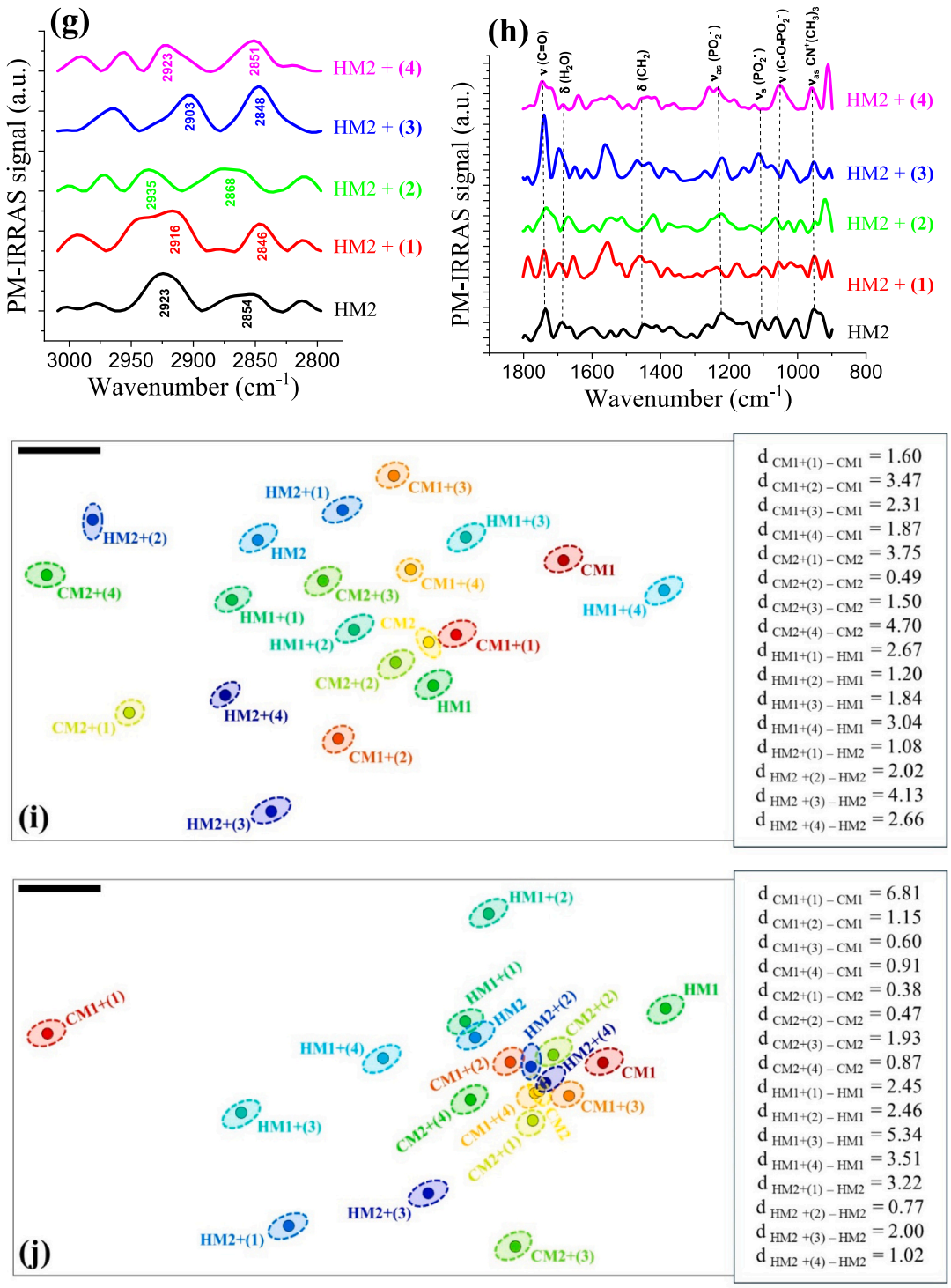


**Fig. 8.** (*continued*).

and in the tails, in the 2800–3000 $cm^{-1}$ region. A detailed discussion of the spectra in Fig. 8 is provided in SI, and for the comparison of effects from the four complexes, one may concentrate on the IDMAP plots in Fig. 8i and j. In the tail region, complex **(2)** and **(3)** caused the highest changes for the CM1 model, whereas for the CM2 model, complexes **(1)** and **(4)** affected it the most. Regarding healthy membrane models, HM1 and HM2 exhibited the largest changes due to complex **(4)** and **(3)**, respectively. For the headgroup region, complex **(1)** and **(3)** had the largest effect on CM1 and CM2, while for HM1 and HM2 the largest changes were induced by complex **(3)** and **(1)**, respectively. In summary, the molecular-level interactions inferred from the PM-IRRAS data do not allow for correlating the effects induced by the complexes on the CM1, CM2, HM1, and HM2 monolayers to their toxicity. Furthermore, we may conclude that the interaction is determined by the type of lipid used in the models, with each complex exhibiting distinct interactions with both saturated and unsaturated lipids.

## 4. Conclusion

Four ruthenium-arene complexes were shown to interact with Langmuir monolayers representing healthy (HM1 and HM2) and cancerous cell (CM1 and CM2) membranes, with changes in the monolayers packing observed in surface pressure isotherms and on PM-IRRAS measurements. In fact, the PM-IRRAS spectra indicate that the four complexes affect the headgroup region as well as the tails of the monolayer molecules. The changes induced by the complexes varied in ways that could not be correlated with their toxicity, as their impact on the Langmuir monolayers is determined by both the nature of the ruthenium complexes and the composition of the membrane models. This conclusion was reached by comparing the data from the surface pressure isotherms, including the compressional moduli and interaction energies, from BAM images and PM-IRRAS for CM1, CM2, HM1, and HM2 incorporating three concentrations of the complexes. The robustness of this conclusion was confirmed by treating the surface pressure isotherms and PM-IRRAS spectra with the multidimensional projection technique IDMAP. From the IDMAP plots we also observed that the cytotoxicity data of these *p*-cymene ruthenium complexes is unrelated to their effect on the proposed cancer and healthy models. For example, complex **(1)** considerably affected all studied models, even though it was the least cytotoxic. The overall results revealed that the mode of action of the ruthenium complexes is not limited to their incorporation into the cell membrane. Therefore, the information provided here may help in understanding how the ruthenium complexes either cross or penetrate the cell membrane. Furthermore, our findings feature the importance of studying lipid membranes in conjunction with other biomolecules in order to determine the primary biological target of metallodrugs. It may also be helpful for the development of other metallodrugs with different types of ligand substitution that will specifically interact with the plasma membrane.

## CRediT authorship contribution statement

**Ellen C. Wrobel:** Writing – review & editing, Writing – original draft, Visualization, Methodology, Investigation, Formal analysis, Data curation, Conceptualization. **Ivelise Dimbarre Lao Guimarães:** Investigation, Formal analysis, Data curation. **Karen Wohnrath:** Writing – review & editing, Visualization, Investigation, Formal analysis. **Osvaldo N. Oliveira:** Writing – review & editing, Supervision, Resources, Funding acquisition, Conceptualization.

## Declaration of competing interest

The authors declare that they have no known competing financial interests or personal relationships that could have appeared to influence the work reported in this paper.

## Acknowledgments

This work was supported by São Paulo Research Foundation (FAPESP) (2020/15571-7 and 2018/22214-6), INEO, CNPq (401271/2014-5), and CAPES.

## Appendix A. Supplementary data

Supplementary data to this article can be found online at https://doi.org/10.1016/j.bbamem.2024.184332.

## References

[1] N. Arshad, S.I. Farooqi, Cyclic voltammetric DNA binding investigations on some anticancer potential metal complexes: a review, Appl. Biochem. Biotechnol. 186 (2018) 1090–1110, https://doi.org/10.1007/s12010-018-2818-z.
[2] J.J. Soldevila-Barreda, N. Metzler-Nolte, Intracellular catalysis with selected metal complexes and metallic nanoparticles: advances toward the development of catalytic metallodrugs, Chem. Rev. 119 (2019) 829–869, https://doi.org/10.1021/acs.chemrev.8b00493.
[3] P. Sudhindra, S. Ajay Sharma, N. Roy, P. Moharana, P. Paira, Recent advances in cytotoxicity, cellular uptake and mechanism of action of ruthenium metallodrugs: a review, Polyhedron 192 (2020) 114827, https://doi.org/10.1016/j.poly.2020.114827.
[4] C.S. Allardyce, P.J. Dyson, Metal-based drugs that break the rules, Dalton Trans. 45 (2016) 3201–3209, https://doi.org/10.1039/c5dt03919c.
[5] T.S. Morais, F.C. Santos, T.F. Jorge, L. Côrte-Real, P.J.A. Madeira, F. Marques, M. P. Robalo, A. Matos, I. Santos, M.H. Garcia, New water-soluble ruthenium(II) cytotoxic complex: biological activity and cellular distribution, J. Inorg. Biochem. 130 (2014) 1–14, https://doi.org/10.1016/j.jinorgbio.2013.09.013.
[6] S. Ghosh, Cisplatin: the first metal based anticancer drug, Bioorg. Chem. 88 (2019) 102925, https://doi.org/10.1016/j.bioorg.2019.102925.
[7] S. Dasari, P. Bernard Tchounwou, Cisplatin in cancer therapy: molecular mechanisms of action, Eur. J. Pharmacol. 740 (2014) 364–378, https://doi.org/10.1016/j.ejphar.2014.07.025.
[8] R.G. Kenny, C.J. Marmion, Toward multi-targeted platinum and ruthenium drugs - a new paradigm in cancer drug treatment regimens? Chem. Rev. 119 (2019) 1058–1137, https://doi.org/10.1021/acs.chemrev.8b00271.
[9] L. Zeng, P. Gupta, Y. Chen, E. Wang, L. Ji, H. Chao, Z.S. Chen, The development of anticancer ruthenium(II) complexes: from single molecule compounds to nanomaterials, Chem. Soc. Rev. 46 (2017) 5771–5804, https://doi.org/10.1039/c7cs00195a.
[10] M.A. Pujante-Galián, S.A. Pérez, M.G. Montalbán, G. Carissimi, M.G. Fuster, G. Víllora, G. García, P-cymene complexes of ruthenium(II) as antitumor agents, Molecules 25 (2020) 5063, https://doi.org/10.3390/molecules25215063.
[11] P. Thangavel, B. Viswanath, S. Kim, Recent developments in the nanostructured materials functionalized with ruthenium complexes for targeted drug delivery to tumors, Int. J. Nanomedicine 12 (2017) 2749–2758, https://doi.org/10.2147/IJN.S131304.
[12] E. Alessio, L. Messori, NAMI-A and KP1019/1339, Two Iconic Ruthenium Anticancer Drug Candidates Face-to-Face: A Case Story in Medicinal Inorganic Chemistry, Molecules 24 (2019) 1995, https://doi.org/10.3390/molecules24101995.
[13] K.D. Mjos, C. Orvig, Metallodrugs in medicinal inorganic chemistry, Chem. Rev. 114 (2014) 4540–4563, https://doi.org/10.1021/cr400460s.
[14] J. Pracharova, V. Novohradsky, H. Kostrhunova, P. Štarha, Z. Trávníček, J. Kasparkova, V. Brabec, Half-sandwich Os(ii) and Ru(ii) bathophenanthroline complexes: anticancer drug candidates with unusual potency and a cellular activity profile in highly invasive triple-negative breast cancer cells, Dalton Trans. 47 (2018) 12197–12208, https://doi.org/10.1039/C8DT02236D.
[15] K. Lin, Z.Z. Zhao, H. Ben Bo, X.J. Hao, J.Q. Wang, Applications of ruthenium complex in tumor diagnosis and therapy, Front. Pharmacol. 9 (2018) 1–10, https://doi.org/10.3389/fphar.2018.01323.
[16] Q. Sun, Y. Li, H. Shi, Y. Wang, J. Zhang, Q. Zhang, Ruthenium complexes as promising candidates against lung cancer, Molecules 26 (2021), https://doi.org/10.3390/molecules26154389.
[17] T. Sathiya Kamatchi, M.K. Mohamed Subarkhan, R. Ramesh, H. Wang, J. G. Małecki, Investigation into antiproliferative activity and apoptosis mechanism of new arene Ru(ii) carbazole-based hydrazone complexes, Dalton Trans. 49 (2020) 11385–11395, https://doi.org/10.1039/d0dt01476a.
[18] X. Ge, X. Liu, Z. Tian, S. Chen, X. Liu, L. Guo, P. Gong, B. Ling, X.A. Yuan, Z. Liu, Half-sandwich ruthenium (II) complexes with triphenylamine modified dipyridine skeleton and application in biology/luminescence imaging, Appl. Organomet. Chem. 33 (2019) 1–12, https://doi.org/10.1002/aoc.5171.
[19] Z. Tian, J. Li, S. Zhang, Z. Xu, Y. Yang, D. Kong, H. Zhang, X. Ge, J. Zhang, Z. Liu, Lysosome-targeted chemotherapeutics: half-sandwich ruthenium(II) complexes that are selectively toxic to cancer cells, Inorg. Chem. 57 (2018) 10498–10502, https://doi.org/10.1021/acs.inorgchem.8b01944.
[20] B.M. Blunden, M.H. Stenzel, Incorporating ruthenium into advanced drug delivery carriers - an innovative generation of chemotherapeutics, J. Chem. Technol. Biotechnol. 90 (2015) 1177–1195, https://doi.org/10.1002/jctb.4507.
[21] Z. Deng, P. Gao, L. Yu, B. Ma, Y. You, L. Chan, C. Mei, T. Chen, Ruthenium complexes with phenylterpyridine derivatives target cell membrane and trigger death receptors-mediated apoptosis in cancer cells, Biomaterials 129 (2017) 111–126, https://doi.org/10.1016/j.biomaterials.2017.03.017.
[22] A.C. Alves, D. Ribeiro, C. Nunes, S. Reis, Biophysics in cancer: the relevance of drug-membrane interaction studies, Biochim. Biophys. Acta Biomembr. 2016 (1858) 2231–2244, https://doi.org/10.1016/j.bbamem.2016.06.025.
[23] C. Stefaniu, G. Brezesinski, H. Möhwald, Langmuir monolayers as models to study processes at membrane surfaces, Adv. Colloid Interface Sci. 208 (2014) 197–213, https://doi.org/10.1016/j.cis.2014.02.013.
[24] E.M. Materon, G.F. Nascimento, F.M. Shimizu, A.S. Câmara, B. Sandrino, R. C. Faria, O.N. Oliveira, Role of sphingomyelin on the interaction of the anticancer drug gemcitabine hydrochloride with cell membrane models, Colloids Surf. B Biointerfaces 196 (2020), https://doi.org/10.1016/j.colsurfb.2020.111357.
[25] E.M. Materón, F.M. Shimizu, K. Figueiredo dos Santos, G.F. Nascimento, V.P. N. Geraldo, O.N. Oliveira, R.C. Faria, Membrane model as key tool in the study of glutathione-s-transferase mediated anticancer drug resistance, Biomed. Pharmacother. 145 (2022), https://doi.org/10.1016/j.biopha.2021.112426.
[26] K.F. Santos, E.M. Materón, O.N. Oliveira Jr., Influence of cytochrome P450 3A4 and membrane lipid composition on doxorubicin activity, Colloids Surf. B Biointerfaces 220 (2022) 112886, https://doi.org/10.1016/j.colsurfb.2022.112886.

[27] M. Pedrosa, J. Maldonado-Valderrama, M.J. Gálvez-Ruiz, Interactions between curcumin and cell membrane models by Langmuir monolayers, Colloids Surf. B Biointerfaces 217 (2022), https://doi.org/10.1016/j.colsurfb.2022.112636.

[28] T.M. Nobre, F.J. Pavinatto, L. Caseli, A. Barros-Timmons, P. Dynarowicz-Łatka, O. N. Oliveira, Interactions of bioactive molecules & nanomaterials with Langmuir monolayers as cell membrane models, Thin Solid Films 593 (2015) 158–188, https://doi.org/10.1016/j.tsf.2015.09.047.

[29] B. Sandrino, T.T. Tominaga, T.M. Nobre, L. Scorsin, E.C. Wrobel, B.C. Fiorin, M. P. De Araujo, L. Caseli, O.N. Oliveira, K. Wohnrath, Correlation of [RuCl3(dppb)(VPy)] cytotoxicity with its effects on the cell membranes: an investigation using langmuir monolayers as membrane models, J. Phys. Chem. B 118 (2014) 10653–10661, https://doi.org/10.1021/jp505657x.

[30] B. Sandrino, E.C. Wrobel, T.M. Nobre, L. Caseli, S.R. Lazaro, A.C. Júnior, J. R. Garcia, O.N. Oliveira, K. Wohnrath, Interaction between active ruthenium complex [RuCl3(dppb)(VPy)] and phospholipid Langmuir monolayers: effects on membrane electrical properties, Chem. Phys. Lett. 649 (2016) 29–36, https://doi.org/10.1016/j.cplett.2016.02.023.

[31] A. Sakai, A.P. de Sousa Mesquista, H.B. Nader, C.C. Lopes, W. Nakanishi, K. Ariga, L. Caseli, The lipid composition affects Trastuzumab adsorption at monolayers at the air-water interface, Chem. Phys. Lipids 227 (2020) 104875, https://doi.org/10.1016/j.chemphyslip.2020.104875.

[32] H. Moehwald, G. Brezesinski, From Langmuir monolayers to multilayer films, Langmuir 32 (2016) 10445–10458, https://doi.org/10.1021/acs.langmuir.6b02518.

[33] O.N. Oliveira, L. Caseli, K. Ariga, The Past and the Future of Langmuir and Langmuir–Blodgett Films, Chem. Rev. (2022), https://doi.org/10.1021/acs.chemrev.1c00754.

[34] L. Biancalana, S. Zacchini, N. Ferri, M.G. Lupo, G. Pampaloni, F. Marchetti, Tuning the cytotoxicity of ruthenium(ii) Para-cymene complexes by mono-substitution at a triphenylphosphine/phenoxydiphenylphosphine ligand, Dalton Trans. 46 (2017) 16589–16604, https://doi.org/10.1039/c7dt03385k.

[35] I. Dimbarre Lao Guimarães, F. Marszaukowski, P. Buhrer Rutka, L. Felipe Borge, R. Augusto Pontes Ribeiro, S. Ricardo de Lazaro, P. Castellen, A. Sagoe-Wagner, R. M. Golsteyn, R.T. Boeré, K. Wohnrath, Synthesis, characterization and anticancer activities of cationic η6-p-cymene ruthenium(II) complexes containing phosphine and nitrogenous ligands, Polyhedron 224 (2022) 115980, https://doi.org/10.1016/j.poly.2022.115980.

[36] I.D.L. Guimarães, F. Marszaukowski, R. Ribeiro, S.R. de Lazaro, K.M. de Oliveira, A.A. Batista, P. Castellen, E. Wrobel, J.R. Garcia, R.T. Boeré, K. Wohnrath, Synthesis and characterization of η6-p-cymene ruthenium(II) complexes containing alkyl- and methoxy-substituted triarylphosphines, J. Organomet. Chem. 931 (2021) 121599, https://doi.org/10.1016/j.jorganchem.2020.121599.

[37] A. Muley, K. Selvan, P. Gupta, S. Kumbhakar, Synthesis, structure, spectral, redox properties and anti-cancer activity of ruthenium(II) Arene complexes with substituted Triazole ligands, J. Organomet. Chem. 954–955 (2021) 122074, https://doi.org/10.1016/j.jorganchem.2021.122074.

[38] R. Minghim, F.V. Paulovich, A. de Andrade Lopes, Content-based text mapping using multi-dimensional projections for exploration of document collections, Visualization and Data Analysis 2006 (6060) (2006) 60600S, https://doi.org/10.1117/12.650880.

[39] W. Szlasa, I. Zendran, A. Zalesińska, M. Tarek, J. Kulbacka, Lipid composition of the cancer cell membrane, J. Bioenerg. Biomembr. 52 (2020) 321–342, https://doi.org/10.1007/s10863-020-09846-4.

[40] T. Zech, C.S. Ejsing, K. Gaus, B. De Wet, A. Shevchenko, K. Simons, T. Harder, Accumulation of raft lipids in T-cell plasma membrane domains engaged in TCR signalling, EMBO J. 28 (2009) 466–476, https://doi.org/10.1038/emboj.2009.6.

[41] Y. Zhang, J. Zhang, Q. Li, Y. Wu, D. Wang, L. Xu, Y. Zhang, S. Wang, T. Wang, F. Liu, M.Y. Zaky, S. Hou, S. Liu, K. Zou, H. Lei, L. Zou, H. Liu, Cholesterol content in cell membrane maintains surface levels of ErbB2 and confers a therapeutic vulnerability in ErbB2-positive breast cancer, Cell Communication and Signaling 17 (2019) 1–12, https://doi.org/10.1186/s12964-019-0328-4.

[42] K. Pinkwart, F. Schneider, M. Lukoseviciute, T. Sauka-Spengler, E. Lyman, C. Eggeling, E. Sezgin, Nanoscale dynamics of cholesterol in the cell membrane, J. Biol. Chem. 294 (2019) 12599–12609, https://doi.org/10.1074/jbc.RA119.009683.

[43] P.L. Yeagle, The Membranes of Cells the Membranes of Cells, Third edition, 2016.

[44] H. Koldsø, D. Shorthouse, J. Hélie, M.S.P. Sansom, Lipid clustering correlates with membrane curvature as revealed by molecular simulations of complex lipid bilayers, PLoS Comput. Biol. 10 (2014), https://doi.org/10.1371/journal.pcbi.1003911.

[45] T. Rivel, C. Ramseyer, S. Yesylevskyy, The asymmetry of plasma membranes and their cholesterol content influence the uptake of cisplatin, Sci. Rep. 9 (2019) 1–14, https://doi.org/10.1038/s41598-019-41903-w.

[46] D. Casares, P.V. Escribá, C.A. Rosselló, Membrane lipid composition: effect on membrane and organelle structure, function and compartmentalization and therapeutic avenues, Int. J. Mol. Sci. 20 (2019) 2167, https://doi.org/10.3390/ijms20092167.

[47] H.I. Ingólfsson, M.N. Melo, F.J. Van Eerden, C. Arnarez, C.A. Lopez, T. A. Wassenaar, X. Periole, A.H. De Vries, D.P. Tieleman, S.J. Marrink, Lipid organization of the plasma membrane, J. Am. Chem. Soc. 136 (2014) 14554–14559, https://doi.org/10.1021/ja507832e.

[48] J.H. Lorent, K.R. Levental, L. Ganesan, G. Rivera-Longsworth, E. Sezgin, M. Doktorova, E. Lyman, I. Levental, Plasma membranes are asymmetric in lipid unsaturation, packing and protein shape, Nat. Chem. Biol. 16 (2020) 644–652, https://doi.org/10.1038/s41589-020-0529-6.

[49] G. Van Meer, A.I.P.M. De Kroon, Lipid map of the mammalian cell, J. Cell Sci. 124 (2011) 5–8, https://doi.org/10.1242/jcs.071233.

[50] M.D. Maximino, C.S. Martin, P. Aléssio, Bisphenol a exposure induces multiple effects in DOPC membrane models, J. Mol. Liq. 359 (2022), https://doi.org/10.1016/j.molliq.2022.119253.

[51] Phosphate-buffered saline (PBS), Cold Spring Harb Protoc 2006, 2006, https://doi.org/10.1101/pdb.rec8247 pdb.rec8247.

[52] J.T. Davies, E.K. Rideal, Properties of monolayers, Interfacial Phenomena (1961) 217–281, https://doi.org/10.1016/b978-0-12-206056-4.50009-6.

[53] P. Dynarowicz-Latka, K. Kita, Molecular interaction in mixed monolayers at the air/water interface, Adv. Colloid Interface Sci. 79 (1999) 1–17, https://doi.org/10.1016/S0001-8686(98)00064-5.

[54] G.L. Gaines, The thermodynamic equation of state for insoluble monolayers. I. Uncharged films, J. Chem. Phys. 69 (1978) 924–930, https://doi.org/10.1063/1.436608.

[55] G.L. Gaines, The thermodynamic equation of state for insoluble monolayers. III. Mixed monolayers, J. Colloid Interface Sci. 85 (1982) 16–18, https://doi.org/10.1016/0021-9797(82)90230-2.

[56] S. Nagadome, N.S. Suzuki, Y. Mine, T. Yamaguchi, H. Nakahara, O. Shibata, C. H. Chang, G. Sugihara, Monolayers (Langmuir films) behavior of multi-component systems composed of a bile acid with different sterols and with their 1:1 mixtures, Colloids Surf. B Biointerfaces 58 (2007) 121–136, https://doi.org/10.1016/j.colsurfb.2007.02.017.

[57] F.V. Paulovich, M.L. Moraes, R.M. Maki, M. Ferreira, O.N. Oliveira, M.C.F. De Oliveira, Information visualization techniques for sensing and biosensing, Analyst 136 (2011) 1344–1350, https://doi.org/10.1039/c0an00822b.

[58] S. Hénon, J. Meunier, Microscope at the Brewster angle: direct observation of first-order phase transitions in monolayers, Rev. Sci. Instrum. 62 (1991) 936–939, https://doi.org/10.1063/1.1142032.

[59] D. Vollhardt, Brewster angle microscopy: a preferential method for mesoscopic characterization of monolayers at the air/water interface, Curr. Opin. Colloid Interface Sci. 19 (2014) 183–197, https://doi.org/10.1016/j.cocis.2014.02.001.

[60] C.J. Van Oss, M.K. Chaudhury, R.J. Good, Interfacial Lifshitz-van der Waals and polar interactions in macroscopic systems, Chem. Rev. 88 (1988) 927–941. https://pubs.acs.org/sharingguidelines.

[61] M. Dyck, A. Kerth, A. Blume, M. Lösche, Interaction of the neurotransmitter, neuropeptide Y, with phospholipid membranes: infrared spectroscopic characterization at the air/water interface, Journal of Physical Chemistry B 110 (2006) 22152–22159, https://doi.org/10.1021/jp062537q.

[62] R.D.O. Pedro, A.R. Pereira, O.N. Oliveira Jr., P.B. Miranda, Interaction of chitosan derivatives with cell membrane models in a biologically relevant medium, Colloids Surf. B Biointerfaces 192 (2020) 111048, https://doi.org/10.1016/j.colsurfb.2020.111048.

[63] K. Jochelavicius, A.R. Pereira, A. Fiamingo, T.M. Nobre, S.P. Campana-Filho, O. N. Oliveira, Chitosan effects on monolayers of zwitterionic, anionic and a natural lipid extract from E. Coli at physiological pH, Colloids Surf. B Biointerfaces 209 (2022), https://doi.org/10.1016/j.colsurfb.2021.112146.

[64] A.R. Pereira, F.M. Shimizu, O.N. Oliveira, Cholesterol modulates the interaction between paclitaxel and Langmuir monolayers simulating cell membranes, Colloids Surf. B Biointerfaces 205 (2021) 111889, https://doi.org/10.1016/j.colsurfb.2021.111889.

[65] M. Zaborowska, D. Dziubak, D. Matyszewska, R. Bilewicz, Surface and electrochemical properties of lipid raft model membranes and how they are affected by incorporation of statin, Electrochim. Acta 386 (2021) 138514, https://doi.org/10.1016/j.electacta.2021.138514.

[66] D.M. Telesford, D. Verreault, V. Reick-Mitrisin, H.C. Allen, Reduced condensing and ordering effects by 7-Ketocholesterol and 5β,6β-Epoxycholesterol on DPPC monolayers, Langmuir 31 (2015) 9859–9869, https://doi.org/10.1021/acs.langmuir.5b02539.

[67] P. Wydro, K. Hac-Wydro, Thermodynamic description of the interactions between lipids in ternary langmuir monolayers: the study of cholesterol distribution in membranes, J. Phys. Chem. B 111 (2007) 2495–2502, https://doi.org/10.1021/jp066950.

[68] T. Miyoshi, S. Kato, Detailed analysis of the surface area and elasticity in the saturated 1,2-Diacylphosphatidylcholine/cholesterol binary monolayer system, Langmuir 31 (2015) 9086–9096, https://doi.org/10.1021/acs.langmuir.5b01775.

[69] G.C.M. Ruiz, W.M. Pazin, L.F. do Carmo Morato, O.N. Oliveira, C.J.L. Constantino, Correlating mono- and bilayers of lipids to investigate the pronounced effects of steroid hormone 17α-ethynylestradiol on membrane models of DPPC/cholesterol, J. Mol. Liq. 311 (2020) 113324, https://doi.org/10.1016/j.molliq.2020.113324.

[70] P. Wydro, S. Knapczyk, M. Łapczyńska, Variations in the condensing effect of cholesterol on saturated versus unsaturated phosphatidylcholines at low and high sterol concentration, Langmuir 27 (2011) 5433–5444, https://doi.org/10.1021/la105142w.

[71] D. Marsh, Lateral pressure in membranes, Biochimica et Biophysica Acta - reviews on, Biomembranes 1286 (1996) 183–223, https://doi.org/10.1016/S0304-4157(96)00009-3.

[72] E.C. Wrobel, L.S. De Lara, T.A.S. Do Carmo, P. Castellen, M. Lazzarotto, S.R. De Lázaro, A. Camilo, L. Caseli, R. Schmidt, C.E. Dewolf, K. Wohnrath, The antibacterial activity of: P-tert-butylcalix[6]arene and its effect on a membrane model: molecular dynamics and Langmuir film studies, Phys. Chem. Chem. Phys. 22 (2020) 6154–6166, https://doi.org/10.1039/d0cp00432d.

[73] P.J. Rousseeuw, Silhouettes: a graphical aid to the interpretation and validation of cluster analysis, J. Comput. Appl. Math. 20 (1987) 53–65, https://doi.org/10.1016/0377-0427(87)90125-7.